

Biaxial Strains Mediated Oxygen Reduction Electrocatalysis on Fenton Reaction Resistant L1₀-PtZn Fuel Cell Cathode

Jiashun Liang, Zhonglong Zhao, Na Li, Xiaoming Wang, Shenzhou Li, Xuan Liu, Tanyuan Wang, Gang Lu, Deli Wang, Bing-Joe Hwang, Yunhui Huang, Dong Su, and Qing Li*

PtM alloy catalysts (e.g., PtFe, PtCo), especially in an intermetallic L10 structure, have attracted considerable interest due to their respectable activity and stability for the oxygen reduction reaction (ORR) in proton exchange membrane fuel cells (PEMFCs). However, metal-catalyzed formation of ·OH from H₂O₂ (i.e., Fenton reaction) by Fe- or Co-containing catalysts causes severe degradation of PEM/catalyst layers, hindering the prospects of commercial applications. Zinc is known as an antioxidant in Fenton reaction, but is rarely alloyed with Pt owing to its relatively negative redox potential. Here, sub-4 nm intermetallic L10-PtZn nanoparticles (NPs) are synthesized as high-performance PEMFC cathode catalysts. In PEMFC tests, the L10-PtZn cathode achieves outstanding activity (0.52 A mg_{Pt}⁻¹ at 0.9 V_{iR-free}) and peak power density of 2.00 W cm⁻²) and stability (only 16.6% loss in mass activity after 30 000 voltage cycles), exceeding the U.S. DOE 2020 targets and most of the reported ORR catalysts. Density function theory calculations reveal that biaxial strains developed upon the disorder-order (A1-L1₀) transition of PtZn NPs would modulate the surface Pt-Pt distances and optimize Pt-O binding for ORR activity enhancement, while the increased vacancy formation energy of Zn atoms in an ordered structure accounts for the improved stability.

1. Introduction

Proton exchange membrane fuel cells (PEMFCs) are considered as promising energy conversion devices for electric vehicles, large scale electronic devices, and stationary power sources.[1-3] However, the performance of a PEMFC is severely limited by the sluggish kinetics of oxygen reduction reaction (ORR) at the cathode.^[4] Carbon-supported platinum (Pt/C) nanoparticles (NPs) with sizes of 3-5 nm are commercially used catalysts for ORR.[5,6] Unfortunately, Pt/C suffers from high cost (≈50 000 \$ per kg), limited activity (mass activity ≈ 0.11 A mg_{Pt}⁻¹ at 0.9 V), and poor stability (≈60% activity loss after 30 000 voltage cycles), [7,8] which is far below U.S. Department of Energy (DOE) 2020 targets and strictly hinders the commercialization of PEMFCs. Therefore, highperformance cathode catalysts have been extensively studied including PtM alloys (M = Fe, Co, Ni, etc.), [9,10] nano-structured

J. Liang, S. Li, X. Liu, Prof. T. Wang, Prof. Y. Huang, Prof. Q. Li
State Key Laboratory of Material Processing and Die & Mould Technology
School of Materials Science and Engineering
Huazhong University of Science and Technology
Wuhan, Hubei 430074, China
E-mail: qing_li@hust.edu.cn
Dr. Z. Zhao
School of Physical Science and Technology
Inner Mongolia University
Hohhot 010021, China
Dr. Z. Zhao, Prof. G. Lu
Department of Physics and Astronomy
California State University Northridge

D

The ORCID identification number(s) for the author(s) of this article can be found under https://doi.org/10.1002/aenm.202000179.

[+]Present address: Department of Chemistry and Key Laboratory for Preparation and Application of Ordered Structural Materials of Guangdong Province, Shantou University, Shantou 515063, China

DOI: 10.1002/aenm.202000179

Dr. N. Li, Prof. D. Su Beijing National Laboratory for Condensed Matter Physics Institute of Physics Chinese Academy of Sciences Beijing 100190, China Dr. N. Li, Prof. D. Su Center for Functional Nanomaterials Brookhaven National Laboratory Upton, NY 11973, USA Prof. X. Wang,[+] Prof. B.-J. Hwang Department of Chemical Engineering National Taiwan University of Science and Technology Taipei 10607, Taiwan Prof. D. Wang School of Chemistry and Chemical Engineering Huazhong University of Science and Technology Wuhan, Hubei 430074, China

Northridge, CA 91330, USA

www.advenergymat.de



Pt-based nanocrystals (NCs) (e.g., core/shell structures, [11,12] framework structures [13-16] and nanowires [14,17]), and catalysts derived from earth-abundant metals. [18,19] Among them, the most studied catalysts are those from Pt alloyed with first-row transition metals such as PtNi, [20,21] PtCo, [22,23] and PtFe. [24,25] However, most of these catalysts adopt disordered face-centered cubic (fcc or A1) structures where Pt and M atoms are randomly arranged within the NCs. Under the typical operating conditions of a PEMFC (cell temperature of 60—80 °C, voltage of 0.6–0.8 V, and strong acidic environment), M is easily oxidized and dissolved. Such metal leaching would lead to severe structural damages and the dissolved M ions may further react with $\rm H_2O_2$ and thus degrade the proton exchange membrane (i.e., Nafion). These factors seriously undermine the long-term performance of PEMFCs.

Inspecting the phase diagrams of bimetallic PtM systems, we know that under appropriate conditions (e.g., temperature and atomic ratio), A1-PtM can be converted into ordered tetragonal L1₀-PtM (with Pt:M ratio of 1:1) structures with much improved stability against the oxidation and acid etching of M. [26-28] For example, L1₀-PtFe, [29,30] L1₀-PtCo, [31,32] and L1₀-PtNi[33] intermetallic NPs have exhibited encouraging ORR activity and stability in PEMFCs. Nevertheless, these redox-active metals, especially Fe, will promote the formation of reactive oxygen species (ROS, like ·OH radical) from H₂O₂ (the main byproduct of 2e⁻ ORR), which is so-called Fenton reaction. The ROS may further degrade the Nafion membrane and catalyst layers.[34] Compared to these metals, Zinc (Zn) receives much limited interests when alloying with Pt, possibly due to its relatively negative redox potential (Zn²⁺/Zn, -0.76 V versus standard hydrogen electrode). Therefore the common reducing agents cannot reduce Zn efficiently and the preparation of PtZn alloy is challenging, even though the structurally ordered L1₀-PtZn catalyst may possess several advantages over other L10-PtM ones. First, it has been well recognized in biochemical systems that the antioxidant properties of Zn could significantly restrain the Fenton reaction.^[35] Second, from the perspective of strain modulation, when PtZn alloy transforms into ordered L1₀-PtZn, the crystal expands along <100> and <010> directions and shrinks along <001> direction (e.g., a = b = 4.025 Å, c =3.491 Å for L1₀-PtZn), which will induce biaxial strains over Pt shell. Such co-existing tensile and compressive strains may be beneficial for ORR activity by favorably modulates the Pt surface strain and Pt-O binding strength. For example, core/ shell PtPb/Pt nanoplates, [36] and PdCu/PtCu NPs[37] under biaxial strains show much improved ORR activity compared to the commercial Pt/C. Moreover, the formation energy of L10-PtZn is much lower than that of L10-PtNi, L10-PtCo, and L1₀-PtFe (-0.566 eV per atom for L1₀-PtZn, -0.24 eV per atom for L1₀-PtFe, -0.096 eV per atom for L1₀-PtNi, and -0.088 eV per atom for L1₀-PtCo, adapted from Materials project database), which may render a significantly improved structural stability to L1₀-PtZn.^[27,28]

In this paper, we develop sub-4 nm L1₀-PtZn/Pt NPs as active and durable ORR electrocatalysts for the first time via a self-protection method. Since high temperature annealing (>600 °C) is generally required to overcome the diffusion barrier and fulfill the A1-L1₀ conversion, MgO^[29,38] or SiO₂^[39,40] are often used as robust protectors against NP aggregation. Nevertheless, such

protective shells would confine the mobility of Pt/M atoms and also make the synthesis much complicated.^[29] Here we employ a 3D Pt@ZnO matrix as a precursor to prepare ultrasmall (3 nm) L1₀-PtZn NPs, which can not only prevent the NP aggregation but also promote the phase transition by creating abundant O vacancies during reductive annealing. The obtained L10-PtZn electrocatalyst with a "Pt-skin" structure demonstrates outstanding activity and stability in PEMFC tests, which outperforms most of the reported PtM ORR catalysts. Mechanistic analysis reveals that the A1 to L10 transition of PtZn leads to biaxial strains over Pt shells, with tension along <110> direction and compression along <101> and <011> ones. The biaxial strains could optimize the binding energy between Pt and oxygenated intermediates with enhanced ORR activity. The A1 to L1₀ transition also increases the vacancy formation energy of Zn atoms, accounting for the much improved structural stability.

2. Results and Discussion

Sub-4 nm L10-PtZn NPs were obtained by annealing Pt NPs encapsulated in ZnO matrix (Pt@ZnO) as a precursor, which was synthesized by a one-pot seed-mediated approach (Figure 1a). Typically, 2.5 nm Pt seeds were synthesized by the reduction of Pt acetylacetonate (Pt(acac)2) in the presence of oleylamine (OAm) and borane tert-butylamine (BTB), followed by coating Pt NPs with ZnO matrix through thermal decomposition of Zn(acac)₂ in the presence of Tri-n-Octylphosphine oxdie (TOPO) and OAm. The effect of reducing agent is also examined, and it seems that BTB is a key to preparing monodisperse 2.5 nm Pt NPs (Figure S1, Supporting Information). The Pt@ZnO matrix was then annealed at 600 °C for 2 h under Ar + 5% H₂. After acid washing to remove the excessive ZnO and loading onto carbon (Vulcan XC72), ordered L10-PtZn NPs were obtained (denoted as L10-PtZn-C). To construct a "Pt-skin" structure on L10-PtZn NPs for improving their high temperature stability, L1₀-PtZn NPs were immersed in the warm (60 °C) 0.1 м HClO₄ solution for another 3 h to remove surface Zn, followed by annealing at 400 °C under Ar + 5% H₂ for 1 h (denoted as L1₀-PtZn/Pt-C, Figure S2, Supporting Information). The disordered A1-PtZn NPs are also synthesized by reacting Pt(acac)₂ and Zn(acac)₂ at 320 °C (Figure S2, Supporting Information, see Experimental Section for details).

As shown in the transmission electron microscopy (TEM) images (Figure 1b and Figure S3, Supporting Information), the average diameter of the Pt NPs was determined to be 2.5 ± 0.3 nm with a narrow size distribution. The inter-plane spacing of the lattice fringes is about 0.225 nm (Figure 1b inset), corresponding to the (111) facet of fcc Pt. High-angle annular dark-field scanning TEM (HAADF-STEM) images of the Pt@ZnO composite (Figure 1c and Figure S4, Supporting Information) show that all Pt NPs are well encapsulated in the ZnO matrix without NP aggregation, as clearly indicated by the high (Pt) and low (Zn) Z contrasts. Interestingly, some strips likely relating to the mesopores can be observed in ZnO matrix. Figure S5, Supporting Information shows the XRD pattern of the as-prepared Pt@ZnO matrix. The diffraction peaks corresponding to crystal planes of ZnO are evident, while the peaks

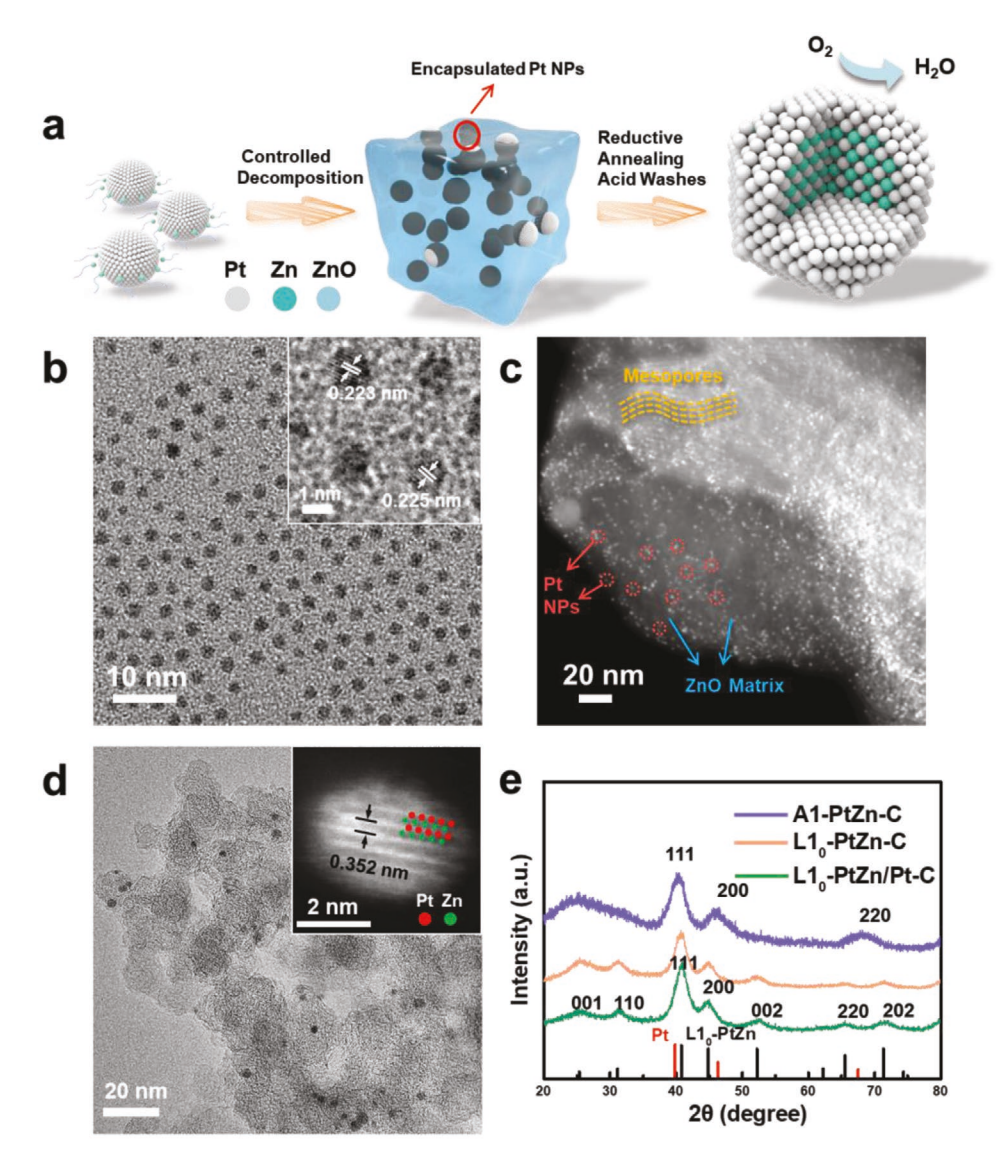


Figure 1. a) Schematic illustration of the synthetic route to L1₀-PtZn/Pt. b) TEM image of the as-prepared Pt NPs. Inset: High-resolution TEM image of Pt NPs. c) HAADF-STEM image of Pt@ZnO matrix. d) TEM image of L1₀-PtZn-C after thermal annealing at 600 °C. Inset: HAADF-STEM image of a representative L1₀-PtZn NP. e) XRD patterns of A1-PtZn-C, L1₀-PtZn-C, and L1₀-PtZn/Pt-C.

of Pt are hardly identified due to the high ratio of ZnO/Pt (20:1). X-ray photoelectron spectroscopy (XPS) was employed to investigate the interaction between Pt and ZnO matrix (Figure S6, Supporting Information). The binding energy of Pt 4f_{7/2} peak of Pt@ZnO sample (70.9 eV) is slightly lower than that of Pt/C (71.4 eV), [41] indicating an possible electron transfer from ZnO to Pt.[42] Such interaction may stabilize Pt NPs during thermal annealing. TOPO plays an important role in controlling the formation of Pt@ZnO matrix. If Zn(acac), decomposed into ZnO in the absence of TOPO, the morphology was less controlled and only a partial Pt NPs could be encapsulated (Figure S7, Supporting Information). It is assumed that TOPO tends to bind with Zn²⁺ and decelerate the decomposition process, thereby controlling the nucleation rate of ZnO to encapsulate the Pt NPs.^[43] After annealing, the size of L1₀-PtZn NPs slightly increases to 3.5 nm due to the incorporation of Zn (Figure 1d and Figure S8, Supporting Information). The ordered structure is clearly identified by the high (Pt) and low (Zn) Z-contrast with Pt and Zn arranging alternatively (Figure 1d inset). The spacing of lattice fringes is measured to be 0.352 nm, corresponding to the (001) facet of L1₀-PtZn. From the Pt 4f XPS spectra of L1₀-PtZn-C, it can be observed that the binding energy of Pt 4f_{7/2} peak exhibits a positive shift compared to Pt/C (from 71.4 to 72 eV), suggesting a down-shift of the *d*-band center after the incorporation of Zn.^[44,45] Such change in the surface electronic structure of Pt could weaken the binding between Pt and oxygenated intermediates, leading to the ORR activity enhancement.^[46]

It is worth noting that the ZnO matrix can serve as a bifunctional component during annealing. Upon reductive annealing, ZnO matrix is partially reduced to Zn and inter-diffuses with Pt to form the L1 $_0$ -PtZn structure. During this process O vacancies are created and the atomic diffusion process can be promoted. [29] Also ZnO matrix can serve as a physical barrier to



www.advenergymat.de

prevent the NP aggregation without additional oxide protectors (e.g., MgO and SiO_2). When annealing in the absence of ZnO matrix, NPs would suffer from severe aggregation and the particle size increases sharply up to 30 nm (Figure S9, Supporting Information). Such self-protection method can be also applied to prepare other ultrasmall PtM (M = Ga, Cu) NPs, further demonstrating its versatility (Figure S10, Supporting Information).

As shown in Figure 1e, X-ray diffraction (XRD) pattern of A1-PtZn-C NPs reveals a typical fcc feature. The diffraction peaks show a slight right-shift compared to pure Pt due to the incorporation of smaller atom (Zn), which may induce a compressive strain in PtZn crystals over Pt shells. After annealing at 600 °C, the XRD pattern of L1₀-PtZn-C NPs is completely different from fcc type and matches well with that of the tetragonal L1₀-PtZn (PDF# 06–0604). The diffraction peaks at \approx 25.7° and \approx 31.5° can be assigned to (001) and (110) superlattice peaks of L1₀-PtZn, respectively. The L1₀-PtZn/Pt-C NPs also show similar tetragonal diffraction patterns with that of L1₀-PtZn-C,

indicating that post treatment would not change the crystal structure. The intensity ratio of (110)/(111) peaks, which reflects the degree of ordering, $^{[47]}$ is measured to be 0.290 and close to that of bulk L10-PtZn (0.30), indicating a high ordering degree of L10-PtZn-C. The particle sizes of the developed samples are calculated to be $\approx\!\!4$ nm by Debye–Scherrer equation, in good agreement with TEM results. The final atomic ratios of Pt/Zn are $\approx\!\!54/46$ and 55/45 for L10-PtZn-C and A1-PtZn-C, respectively, as determined by X-Ray fluorescence (XRF) (Figure S11, Supporting Information). After post acid washing, the Pt/Zn ratio of L10-PtZn/Pt NPs changes to 70/30 (Figure S11, Supporting Information), which is a reasonable result considering the ultrasmall particle size.

Cyclic voltammetry (CV) and linear scanning voltammetry are carried out to evaluate the electrochemical performance of the L1₀-PtZn-C, A1-PtZn-C, and commercial Pt/C catalysts in a three-electrode system (details see SI). CV curves of different samples in N₂-saturated 0.1 M HClO₄ solution are shown in

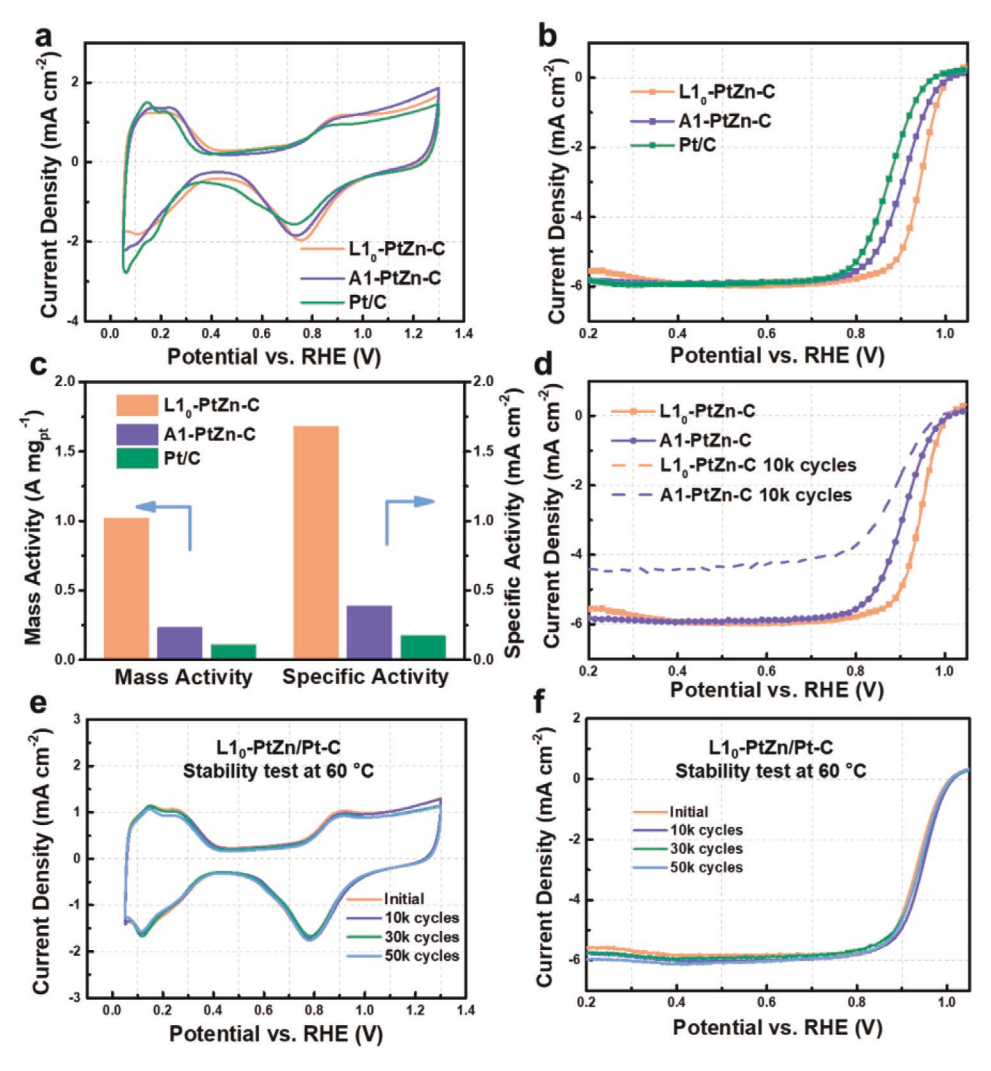


Figure 2. a) CV curves of L1 $_0$ -PtZn-C, A1-PtZn-C, and Pt/C in N $_2$ -saturated 0.1 M HClO $_4$ (scan rate, 50 mV s $^{-1}$). b) ORR polarization curves of L1 $_0$ -PtZn-C, A1-PtZn-C, and Pt/C in O $_2$ -saturated 0.1 M HClO $_4$ (rotating speed, 1600 rpm; scan rate, 10 mV s $^{-1}$). c) MA and SA of L1 $_0$ -PtZn-C, A1-PtZn-C, and Pt/C at 0.9 V. d) ORR polarization curves of L1 $_0$ -PtZn-C, A1-PtZn-C, and Pt/C in O $_2$ -saturated 0.1 M HClO $_4$ before and after ADT at RT. e) CV curves of L1 $_0$ -PtZn/Pt-C in N $_2$ -saturated 0.1 M HClO $_4$ before and after ADT at 60 °C. f) ORR polarization curves of L1 $_0$ -PtZn/Pt-C in O $_2$ -saturated 0.1 M HClO $_4$ before and after ADT at 60 °C.



Figure 2a. According to the charge associated with absorption and desorption of hydrogen (H_{upd}), the electrochemically active surface areas (ECSAs) of the catalysts are calculated to be 61.1, 61.9, and 62.7 $\text{m}^2\ \text{g}_{\text{Pt}}^{-1}$ for L1₀-PtZn-C, A1-PtZn-C, and Pt/C, respectively. Figure 2b presents the ORR polarization curves of three studied catalysts in O2-saturated 0.1 M HClO4 with same Pt loadings. The half-wave potential $(E_{1/2})$ of Pt/C for ORR is 0.872 V versus reversible hydrogen electrode. When Pt alloyed with Zn to form A1-PtZn, the ORR polarization curve exhibits a positive shift in $E_{1/2}$ to 0.904 V. This activity enhancement can be ascribed to a combination of ligand effect and strain effect induced by Zn incorporation, which can weaken the adsorption energy between Pt and O species.^[48] After the phase transition from A1 to L1₀, the $E_{1/2}$ dramatically increases to 0.943 V. Meanwhile, L1₀-PtZn-C demonstrates an excellent mass activity (MA) of 1.02 A mg_{Pt}⁻¹ and a specific activity (SA) of 1.68 mA cm⁻² at 0.9 V (Figure 2c), respectively, which outperforms the A1 counterpart and reveals 9.3- and 9.6-time improvements compared to that of the commercial Pt/C (0.11 A mg_{Pt}⁻¹ and 0.175 mA cm⁻²), respectively. The H₂O₂ yield during ORR catalyzed by L1₀-PtZn-C is measured (by rotating ring/disk electrode) to be 1-2% (Figure S12, Supporting Information), further attesting the high selectivity of L10-PtZn-C on catalyzing ORR via a fourelectron process.

The stability of different samples is evaluated by accelerated durability testing (ADT, potential cycles between 0.6 and 1.0 V in O2-saturated 0.1 M HClO4) at both room temperature (RT) and 60 °C. After 10 000 potential cycles at RT, both A1-PtZn-C and Pt/C suffer from severe degradation with 15 and 26 mV $E_{1/2}$ loss, respectively (Figure 2d and Figure S13, Supporting Information). In the contrast, L10-PtZn-C demonstrates an excellent stability with no obvious shift in $E_{1/2}$ and negligible loss in MA and SA (Figure 2d and Figure S14, Supporting Information). TEM image of L1₀-PtZn-C after ADT shows no obvious morphology change (Figure S15, Supporting Information). As a PEMFC is typically operating at 60-80 °C, it is essential to evaluate the stability of catalysts at an elevated temperature. Despite that the L1₀-PtZn-C catalyst shows enhanced stability at RT, it suffers from quite severe activity degradation after 10 000 potential cycles at 60 °C (Figure S16, Supporting Information). Remarkably, constructing a "Pt-skin" structure on L10-PtZn NPs can dramatically improve the stability at 60 °C. L1₀-PtZn/ Pt-C only exhibits 14% loss in ECSA and 8 mV loss in $E_{1/2}$ even after 50 000 cycles at 60 °C (Figure 2e,f). After 50 000 cycles, the ratio of Pt/Zn in L10-PtZn/Pt-C slightly changes from 70/30 to 77/23 without obvious morphology change (Figure S17, Supporting Information).

Spherical aberration (Cs)-corrected HAADF-STEM and energy dispersive X-ray elemental mapping are employed for analyzing the catalyst structure after ADT. A representative L1₀-PtZn NP after 10 000 cycles at RT is viewed along the [11-2] zone axis (**Figure 3**a). The atomic model is presented on the experimental image and it is in good agreement with that of standard L1₀-PtZn crystal view along [11-2] direction (Figure 3b). The ordered structure of L1₀-PtZn NP is indicated by the high (Pt) and low (Zn) Z contrasts and their alternative arrangement along <1-10> direction (Figure 3a and Figure S18, Supporting Information). Inset of Figure 3a represents the corresponding fast Fourier transformation (FFT) pattern of this NP, showing the presence of (110)

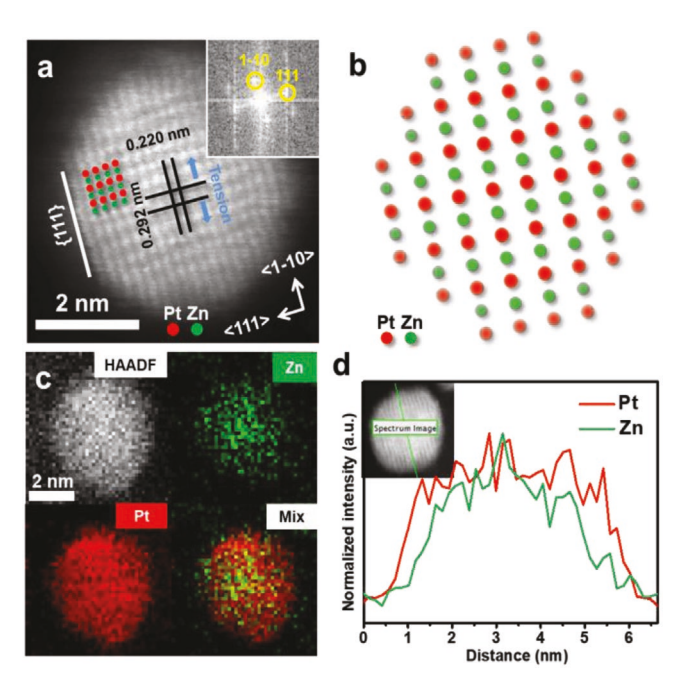


Figure 3. a) HAADF-STEM image of a $L1_0$ -PtZn NP. Inset in (a), the corresponding FFT pattern. b) Standard atomic arrangement of $L1_0$ -PtZn view along [11-2] direction. c) Elemental mappings of Pt and Zn. d) STEM-EELS line-scan profile of a $L1_0$ -PtZn NP.

superlattice spots. These features firmly prove the presence of ordered L1₀ structure. This unique periodic L1₀ structure may induce a strong interaction between Pt and Zn, thereby increase the stability of Zn against acid. Besides, the spacings of lattice fringes are measured to be 0.292 and 0.220 nm, corresponding to (110) and (111) facets, respectively. The lattice spacing of (110) facet, corresponding to d_{Pt-Pt} in L1₀-PtZn, is larger than that in A1-Pt (0.277 nm), indicating a tensile strain along <110> direction. Viewed in another direction, the lattice spacing of (011) facet, corresponding to $d_{\text{Pt-Zn}}$, is about 0.270 nm, showing a compressive strain along <011> direction (Figure S19, Supporting Information). In this regard, these observations provide experimental evidences for biaxial strains in L1₀-PtZn NPs. According to the elemental mapping and STEM-electron energy loss spectroscopy (STEM-EELS) line scans of a single NP (Figure 3c,d), core/ shell structure with Pt-rich shell and homogenous PtZn core is observed, indicating the slightly etching of Zn during acid treatment or potential cycles. The thickness of Pt shell is ≈0.6 nm, corresponding to ≈ 3 atomic layers.

The membrane electrodes assembly equipped with L1₀-PtZn/Pt-C cathode is fabricated to evaluate its performance in a PEMFC. **Figure 4**a presents the H₂-O₂ fuel cell polarization curves (i–V) of the commercial Pt/C and L1₀-PtZn/Pt-C at 80 °C. L1₀-PtZn/Pt-C reveals an encouraging performance in the kinetic range (0.549 A cm⁻² at 0.8 V), which is much improved compared to that of commercial Pt/C. The maximum peak power density for L1₀-PtZn/Pt-C reaches as high as 2.00 W cm⁻², which is superior to most of other reported PtM cathode. Noteworthy, L1₀-PtZn/Pt-C catalyst demonstrates extraordinarily high durability in PEMFC cathode. The i–V curve shows negligible change after 30 000 voltage cycles from 0.6 to 0.95 V at 100 mV s⁻¹ in N₂ atmosphere (Figure 4b). By

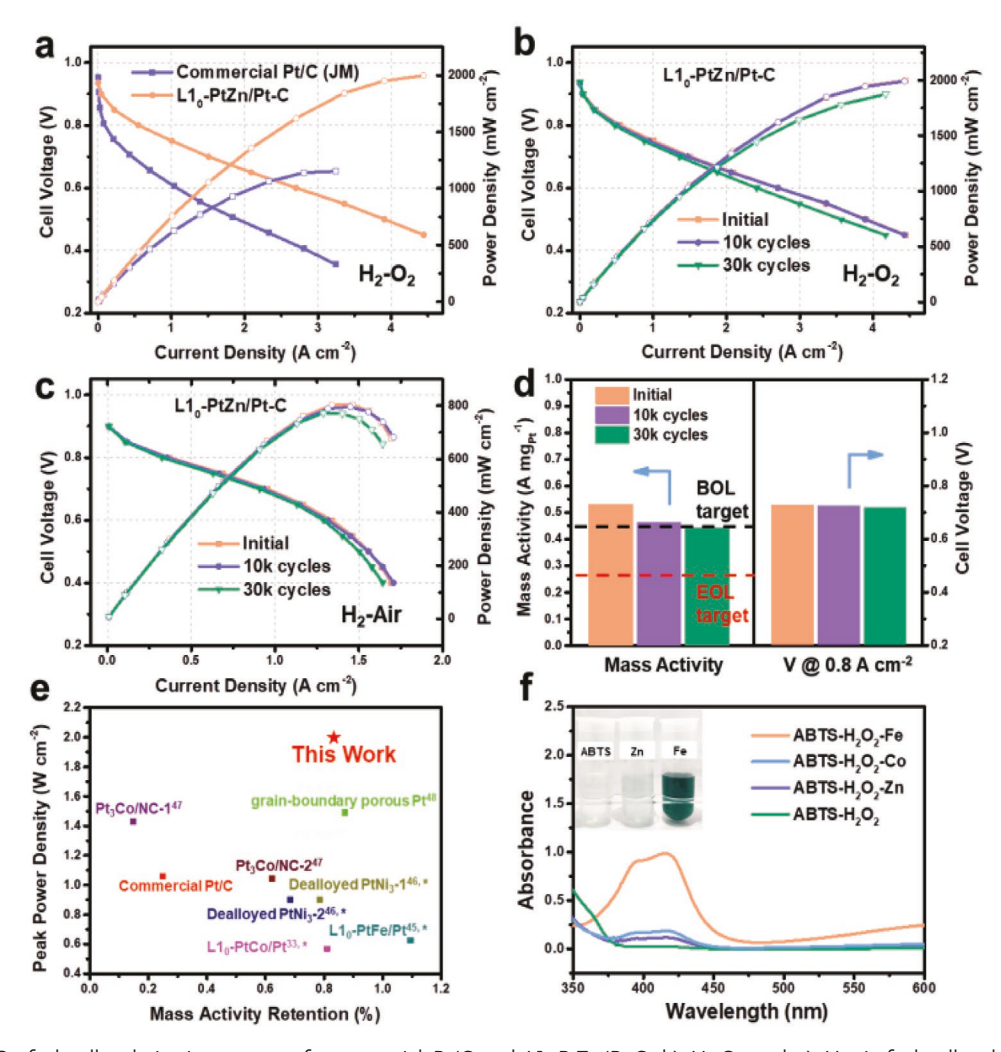


Figure 4. a) H_2 - O_2 fuel cell polarization curves of commercial Pt/C and $L1_0$ -PtZn/Pt-C. b) H_2 - O_2 and c) H_2 -air fuel cell polarization curves of $L1_0$ -PtZn/Pt-C after 30 000 voltage cycles. Anode: 0.1 mg_{Pt} cm⁻² 20% Pt/C; cathode: 0.104 mg_{Pt} cm⁻² $L1_0$ -PtZn/Pt-C or 0.16 mg_{Pt} cm⁻² 20% Pt/C; membrane: Nafion 211; temperature: 80 °C; backpressure: 150 kPa. d) Changes of MA and voltage at 0.8 A cm⁻² of $L1_0$ -PtZn/Pt-C before and after voltage cycles (black and red dash lines indicate the DOE beginning-of-life (BOL) and end-of-life (EOL) targets, respectively). e) Comparison of the mass activity retention and peak power density for catalysts between this work and previous ones. Footnote*: The power density was evaluated from i-V curves under H_2 -air condition. (f) UV/V absorption spectra of 0.1 M $HCIO_4$ solutions of ABTS- H_2O_2 and after the additions of Fe, Co, Zn. Inset: photographs showing the color change of the solution after the Fenton reaction.

contrast, Pt/C catalyst suffers from quite severe performance loss after 30 000 cycles (Figure S20, Supporting Information). The performance before and after voltage cycling is further quantified using the MA at 0.9 V_{iR-free} as suggested by DOE (Figure 4d). The L1₀-PtZn/Pt-C catalyst achieves an initial MA of 0.52 A mg_{Pt}⁻¹ and only 16.6% MA loss after 30 000 cycles, surpassing the DOE 2020 targets on both MA (0.44 A mg_{pt}⁻¹) and MA loss (<40% after 30 000 cycles). When feeding with air, our L10-PtZn/Pt-C catalyst also demonstrates promising performance as well as high stability after 30 000 cycles (Figure 4c), holding great potential in PEMFC applications. Specifically, the initial current density at 0.8 V is 372 mA cm⁻², meeting DOE 2020 target (300 mA cm $^{-2}$ at 0.8 V). After 30 000 potential cycles, less than 10 mV voltage loss can be observed at the current density of 0.8 A cm⁻² (Figure 4d). The excellent performance in activity and stability makes our L10-PtZn/Pt-C among the most competitive ORR catalysts in PEMFCs (Figure 4e).[32,49-52] In addition to the stability of catalyst itself, the degradation of Nafion membrane caused by ROS may also lead to stability issues. We therefore assess the ROS production level by UV–vis absorption spectroscopy with 2, 20-azinobis (3-ethylbenzthiazoline-6-sulfonate) (ABTS) as substrate. Figure 4f shows that the absorbance value of ABTS-H₂O₂-Zn is lower than that of ABTS-H₂O₂-Co and ABTS-H₂O₂-Fe, thus unambiguously demonstrating that Zn could significantly restrain the Fenton reaction and the formation of ROS.

The enhanced activity of L1₀-PtZn/Pt-C catalysts is further interpreted in terms of Pt strain. Based on TEM and HAADF-STEM results, a (111) facet slab model of L1₀-PtZn/Pt is constructed, as shown in **Figure 5**a. When A1 structure transforms into L1₀ structure, the lattice constants change significantly with expansion along <100>, <010> directions and compression along <001> one. Therefore, the Pt–Pt distance ($d_{\text{Pt-Pt}}$) increases to 2.837 Å while the Pt–Zn distance ($d_{\text{Pt-Zn}}$) shrinks

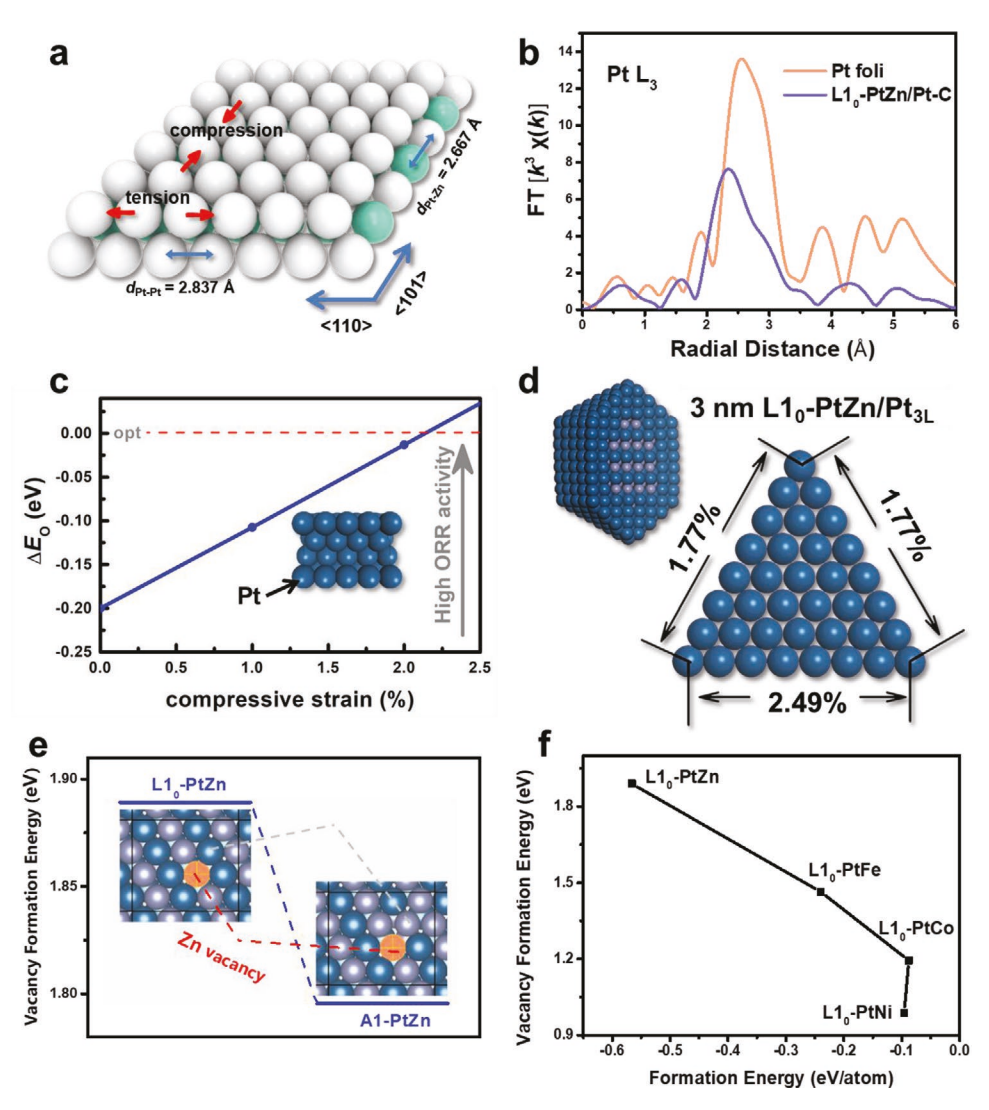


Figure 5. a) Schematic illustration of lattice mismatch between L1₀-PtZn core and A1-Pt shell. White and green spheres represent Pt and Zn atoms, respectively. b) Pt L3 k^3 -weighted FT-EXAFS spectra of Pt foil, and L1₀-PtZn/Pt-C. c) ΔE_O as a function of compressive strain on the (111) surface. The optimal E_O is set to zero. d) Simulation model of 3-nm L1₀-PtZn/Pt3_L NP and strain distribution on the (111) surface of L1₀-PtZn/Pt. e) Vacancy formation energy of Zn atom for ordered and disordered PtZn slabs. f) Correlations between the formation energy and vacancy formation energy of M in various L1₀-PtM systems.

to 2.667 Å, far different from the d_{Pt-Pt} (2.775 Å) in pure A1-Pt (Figure 5a and Figure S21, Supporting Information). The mismatch between A1 Pt shell and L10-PtZn core will induce biaxial strains on a coherent interface consequently. As shown in Figure 5a; Figure S21 and Table S1, Supporting Information, tensile strain up to 2.23% along <110> direction is created upon Pt (111) facet. While along <011> and <101> directions, compressive strain up to 3.9% emerges. The model analysis is in good agreement with the observation in microscopy results. To make the comparison, the lattice mismatches of L1₀-PtFe/ Pt, which is a widely reported ORR catalytic system, are also calculated with compression along three directions (Figure S21 and Table S1, Supporting Information). The lattice mismatches are similar along <011> and <101> directions, while tension arises in L1₀-PtZn/Pt along <110> direction. Considering that the surface strain is overcompressed in L1₀-PtFe/Pt in previous report,[54] the biaxial strains in L10-PtZn/Pt may shorten the

Pt–Pt distance and favorably modulate the strain over Pt surface synergistically, thereby promoting the ORR activity based on strain effect.^[48,55,56]

To verify our hypothesis, extended X-ray absorption fine structure (EXAFS) spectroscopy and density function theory (DFT) calculations are employed. EXAFS results reveal that the Pt–Pt bond length in L1₀-PtZn/Pt-C (2.730 Å) is shorter than that of Pt foil (2.765 Å) (Figure 5b; Figure S22 and Table S1, Supporting Information) and indeed longer than that of L1₀-PtFe/Pt (2.675 Å). [49] The shortened Pt–Pt bond and the resultant strain on the surface could weaken the oxygen adsorption energy (E_0), accounting for the enhanced ORR activity. [48,55,56]

DFT calculations are performed to elucidate the origin of enhanced ORR activity on the PtZn/Pt core/shell NPs. We find that the chemical bonding is strengthened when Zn is introduced to Pt. The Bader charge analysis reveals significant charge transfer from Zn to Pt (\approx 0.6 e per atom) in both ordered



ENERG

www.advancedsciencenews.com www.advenergymat.de EXAFS and DFT results reveal that A1 to L10 transition of PtZn and disordered PtZn alloys, leading to a strong ionic/metallic leads to biaxial strains over Pt shell, with tension along <110> direction and compression along <101> and <011> directions, thereby arising favorable compressive strain on Pt-skin toward high ORR activity. PEMFC tests demonstrate that L1₀-PtZn/ Pt-C cathode catalyst displays promising activity and stability, with MA of 0.52 A mg_{Pt}⁻¹, peak power density of 2.00 W cm⁻², and only 16.6% loss after 30 000 potential cycles, outperforming most of the reported PEMFC cathodes with an outstanding activity-stability balance. Such excellent PEMFC stability can be attributed to the increased vacancy formation energy of Zn atoms in L10 structure as well as the Fenton reaction resistant effect of antioxidative Zn. This work highlights a low-cost and feasible strategy to develop commercially viable PEFMC cathode catalyst with simultaneous surface strain control and side reaction elimination. Supporting Information Supporting Information is available from the Wiley Online Library or from the author.

binding between Zn and Pt, and shortened lattice parameters. The oxygen adsorption energy on transition metal surfaces, $E_{\rm O}$, has been widely used as a descriptor for ORR activity. [46,57] Here we first calculate $E_{\rm O}$ on Pt (111) surface under biaxial compressions shown in Figure 5c. There is an optimal E_0 value under which the ORR activity reaches the maximum and we use $\Delta E_{\rm O}$ to represent the difference of a given $E_{\rm O}$ value relative to the optimal reference. A linear relationship between $\Delta E_{\rm O}$ and the compressive strain is observed with an optimal compression of 2.13% on Pt (111). We next estimate the surface strain distributions on L1₀-PtZn/Pt and L1₀-PtFe/Pt core/shell NPs as well as pure Pt NP using the Molecular Mechanics modeling approach.^[58] Each NP is modeled by a truncated octahedron with a diameter of ≈3 nm and a Pt shell of 3-atom-layer thickness (≈0.6 nm) as shown in Figure 5d. In the L1₀-PtZn/Pt NP after relaxation, an average compressive strain of 1.77% is developed along <011> and <101> directions and a compressive strain of 2.49% is developed along <110> direction (Figure 5d). Compared to the L1₀-PtFe/Pt NPs, which are over-compressed according to the previous study,^[54] the average surface compression in the L1₀-PtZn/Pt NPs is reduced by ≈14% (Figure S23, Supporting Information), thanks to the expansion in the <110> direction in the L1₀-PtZn core. The release of the over-compression leads to more optimal ΔE_0 . In addition, the average surface strain of the A1-PtZn NPs is much smaller than that of the L1₀-PtZn/Pt NPs (Figure S24, Supporting Information). Thus, the L1₀-PtZn/Pt core/shell NPs are expected to be more active than the A1-PtZn and pure Pt NPs, which is consistent with the experimental trend. Ligand effect is not considered here because it is known to be negligible for a shell thickness greater than two layers.^[59] The insights into how A1 to L1₀ transition boosts the long-term durability of the ordered catalyst for ORR is also investigated. The vacancy formation energy of Zn atom, which refers to the energy required to break the bonds between a Zn atom and its neighboring atoms and move outside the crystal, are calculated and compared for A1- and L10-PtZn catalysts. In the computational model, one of the Pt atoms adjoin to the Zn atom in L1₀-PtZn is replaced by a Zn atom to simulate the agminated Zn-Zn interaction in A1-PtZn. As shown in Figure 5e, the vacancy formation energy of Zn increases by ≈0.1 eV after structural ordering due to the reduced Zn-Zn interactions, suggesting the improved structural stability and oxidation resistance of Zn atoms in the L1₀-PtZn catalyst. We further compare the vacancy formation energy of PtZn with PtM (M = Fe, Co, Ni) in the $L1_0$ structures and plot the results with the corresponding formation energy (Figure 5f). Interestingly, a negative correlation can be observed: the more negative the formation energy of L1₀-PtM is, the higher the vacancy formation energy of M we get, which declare the higher structural stability of L1₀-PtZn/Pt core/shell nanocatalysts among the others.

3. Conclusion

In summary, the antioxidative element Zn is employed to alloy with Pt and sub-4 nm L1₀-PtZn NPs are successfully prepared as a high-performance PEMFC cathode for the first time.

Acknowledgements

J.L. and Z.Z. contributed equally to this work. This work was financial supported by National Nature Science Foundation of China (21972051). The work at California State University Northridge was supported by NSF-PREM program (DMR-1828019). The authors thank the Analytical and Testing Center of Huazhong University of Science and Technology (HUST) for carrying out the ICP-MS, XRF, XPS, and XRD measurements. Electron microscopy work was performed at the Center for Functional Nanomaterials, Brookhaven National Laboratory, which is supported by the U.S. Department of Energy (DOE), Office of Basic Energy Science, under contract No. DE-SC0012704.

Conflict of Interest

The authors declare no conflict of interest.

Keywords

electrocatalysis, Fenton reaction, fuel cells, intermetallics, oxygen reduction

> Received: January 16, 2020 Revised: May 6, 2020 Published online:

- [1] H. A. Gasteiger, N. M. Markovic, Science 2009, 324, 48.
- [2] M. K. Debe, Nature 2012, 486, 43.
- [3] R. Bashyam, P. Zelenay, Nature 2006, 443, 63.
- [4] D. Y. Chung, J. M. Yoo, Y.-E. Sung, Adv. Mater. 2018, 30, 1704123.
- [5] V. R. Stamenkovic, B. S. Mun, M. Arenz, K. J. J. Mayrhofer, C. A. Lucas, G. F. Wang, P. N. Ross, N. M. Markovic, Nat. Mater.
- [6] J. Greeley, I. E. L. Stephens, A. S. Bondarenko, T. P. Johansson, H. A. Hansen, T. F. Jaramillo, J. Rossmeisl, I. Chorkendorff, J. K. Norskov, Nat. Chem. 2009, 1, 552.

www.advenergymat.de

ENERGY

- [7] M. H. Shao, Q. W. Chang, J. P. Dodelet, R. Chenitz, Chem. Rev. 2016. 116, 3594.
- [8] L. Du, V. Prabhakaran, X. Xie, S. Park, Y. Wang, Y. Shao, Adv. Mater. 2020, https://doi.org/10.1002/adma.201908232.
- [9] C. Chen, Y. J. Kang, Z. Y. Huo, Z. W. Zhu, W. Y. Huang, H. L. L. Xin, J. D. Snyder, D. G. Li, J. A. Herron, M. Mavrikakis, M. F. Chi, K. L. More, Y. D. Li, N. M. Markovic, G. A. Somorjai, P. D. Yang, V. R. Stamenkovic, *Science* 2014, 343, 1339.
- [10] N. Becknell, Y. J. Kang, C. Chen, J. Resasco, N. Kornienko, J. H. Guo, N. M. Markovic, G. A. Somorjai, V. R. Stamenkovic, P. D. Yang, J. Am. Chem. Soc. 2015, 137, 15817.
- [11] X. Zhao, S. Chen, Z. C. Fang, J. Ding, W. Sang, Y. C. Wang, J. Zhao, Z. M. Peng, J. Zeng, J. Am. Chem. Soc. 2015, 137, 2804.
- [12] J. Hu, L. Wu, K. A. Kuttiyiel, K. R. Goodman, C. Zhang, Y. Zhu, M. B. Vukmirovic, M. G. White, K. Sasaki, R. R. Adzic, J. Am. Chem. Soc. 2016, 138, 9294.
- [13] N. Becknell, Y. Son, D. Kim, D. G. Li, Y. Yu, Z. Q. Niu, T. Lei, B. T. Sneed, K. L. More, N. M. Markovic, V. R. Stamenkovic, P. D. Yang, J. Am. Chem. Soc. 2017, 139, 11678.
- [14] X. Yang, L. T. Roling, M. Vara, A. O. Elnabawy, M. Zhao, Z. D. Hood, S. Bao, M. Mavrikakis, Y. Xia, *Nano Lett.* **2016**, *16*, 6644.
- [15] X. Wang, L. Figueroa-Cosme, X. Yang, M. Luo, J. Y. Liu, Z. X. Xie, Y. N. Xia, *Nano Lett.* **2016**, *16*, 1467.
- [16] D. S. He, D. He, J. Wang, Y. Lin, P. Yin, X. Hong, Y. Wu, Y. Li, J. Am. Chem. Soc. 2016, 138, 1494.
- [17] K. Jiang, D. Zhao, S. Guo, X. Zhang, X. Zhu, J. Guo, G. Lu, X. Huang, Sci. Adv. 2017, 3, e1601705.
- [18] H. Q. Liu, R. R. Adzic, S. S. Wong, ACS Appl. Mater. Interfaces 2015, 7. 26145.
- [19] Q. Li, P. Xu, W. Gao, S. G. Ma, G. Q. Zhang, R. G. Cao, J. Cho, H. L. Wang, G. Wu, Adv. Mater. 2014, 26, 1378.
- [20] G. Niu, M. Zhou, X. Yang, J. Park, N. Lu, J. Wang, M. J. Kim, L. Wang, Y. Xia, Nano Lett. 2016, 16, 3850.
- [21] V. R. Stamenkovic, B. Fowler, B. S. Mun, G. F. Wang, P. N. Ross, C. A. Lucas, N. M. Markovic, *Science* 2007, 315, 493.
- [22] X. Tan, S. Prabhudev, A. Kohandehghan, D. Karpuzov, G. A. Botton, D. Mitlin, ACS Catal. 2015, 5, 1513.
- [23] B. Xia, H. Wu, N. Li, Y. Yan, X. Lou, X. Wang, Angew. Chem., Int. Ed. 2015. 54, 3797.
- [24] H. Zhu, S. Zhang, D. Su, G. Jiang, S. Sun, Small 2015, 11, 3545.
- [25] C. Wang, Y. Hou, J. Kim, S. Sun, Angew. Chem., Int. Ed. 2007, 46,
- [26] M. C. Luo, Y. J. Sun, L. Wang, S. J. Guo, Adv. Energy Mater. 2017, 7, 1602073.
- [27] Y. C. Yan, J. S. S. Du, K. D. Gilroy, D. R. Yang, Y. N. Xia, H. Zhang, Adv. Mater. 2017, 29, 1806746.
- [28] J. Liang, F. Ma, S. Hwang, X. Wang, J. Sokolowski, Q. Li, G. Wu, D. Su, Joule 2019, 3, 956.
- [29] Q. Li, L. H. Wu, G. Wu, D. Su, H. F. Lv, S. Zhang, W. L. Zhu, A. Casimir, H. Y. Zhu, A. Mendoza-Garcia, S. H. Sun, *Nano Lett.* 2015, 15, 2468.
- [30] X. Du, Y. He, X. Wang, J. Wang, Energy Environ. Sci. 2016, 9, 2623.
- [31] J. Liang, N. Li, Z. Zhao, L. Ma, X. Wang, S. Li, X. Liu, T. Wang, Y. Du, G. Lu, J. Han, Y. Huang, D. Su, Q. Li, Angew. Chem., Int. Ed. 2019, 58, 15471.
- [32] J. Li, S. Sharma, X. Liu, Y.-T. Pan, J. S. Spendelow, M. Chi, Y. Jia, P. Zhang, D. A. Cullen, Z. Xi, H. Lin, Z. Yin, B. Shen, M. Muzzio, C. Yu, Y. S. Kim, A. A. Peterson, K. L. More, H. Zhu, S. Sun, Joule 2019, 3, 124.

- [33] T. Wang, J. Liang, Z. Zhao, S. Li, G. Lu, Z. Xia, C. Wang, J. Luo, J. Han, C. Ma, Adv. Energy Mater. 2019, 9, 1803771.
- [34] A. D. Bokare, W. Choi, J. Hazard. Mater. 2014, 275, 121.
- [35] S. R. Powell, J. Nutr. 2000, 130, 1447S.
- [36] L. Z. Bu, Y. G. Feng, J. L. Yao, S. J. Guo, J. Guo, X. Q. Huang, Nano Res. 2016, 9, 2811.
- [37] C. Y. Wang, X. H. Sang, J. T. L. Gamier, D. P. Chen, R. R. Unocic, S. E. Skrabalak, *Nano Lett.* **2017**, *17*, 5526.
- [38] J. Kim, Y. Lee, S. H. Sun, J. Am. Chem. Soc. 2010, 132, 4996.
- [39] Z. Y. Qi, C. X. Xiao, C. Liu, T. W. Goh, L. Zhou, R. Maligal-Ganesh, Y. C. Pei, X. L. Li, L. A. Curtiss, W. Y. Huang, J. Am. Chem. Soc. 2017, 139, 4762.
- [40] E. W. Zhao, R. Maligal-Ganesh, C. Xiao, T. W. Goh, Z. Qi, Y. Pei, H. E. Hagelin-Weaver, W. Huang, C. R. Bowers, *Angew. Chem., Int. Ed.* 2017, 56, 3925.
- [41] D. S. Choi, A. W. Robertson, J. H. Warner, S. O. Kim, H. Kim, Adv. Mater. 2016, 28, 7115.
- [42] C. George, A. Genovese, A. Casu, M. Prato, M. Povia, L. Manna, T. Montanari, Nano Lett. 2013, 13, 752.
- [43] J. Joo, H. B. Na, T. Yu, J. H. Yu, Y. W. Kim, F. X. Wu, J. Z. Zhang, T. Hyeon, J. Am. Chem. Soc. 2003, 125, 11100.
- [44] M. C. Luo, Z. L. Zhao, Y. L. Zhang, Y. J. Sun, Y. Xing, F. Lv, Y. Yang, X. Zhang, S. Hwang, Y. N. Qin, J. Y. Ma, F. Lin, D. Su, G. Lu, S. J. Guo, *Nature* 2019, 574, 81.
- [45] K. Wang, Y. N. Qin, F. Lv, M. Q. Li, Q. Liu, F. Lin, J. R. Feng, C. Yang, P. Gao, S. J. Guo, Small Methods 2018, 2, 1700331.
- [46] V. Stamenkovic, B. S. Mun, K. J. J. Mayrhofer, P. N. Ross, N. M. Markovic, J. Rossmeisl, J. Greeley, J. K. Norskov, Angew. Chem., Int. Ed. 2006, 45, 2897.
- [47] Z. Cui, H. Chen, M. Zhao, F. J. DiSalvo, Nano Lett. 2016, 16, 2560.
- [48] P. Strasser, S. Koh, T. Anniyev, J. Greeley, K. More, C. F. Yu, Z. C. Liu, S. Kaya, D. Nordlund, H. Ogasawara, M. F. Toney, A. Nilsson, Nat. Chem. 2010. 2, 454.
- [49] J. Li, Z. Xi, Y. T. Pan, J. S. Spendelow, P. N. Duchesne, D. Su, Q. Li, C. Yu, Z. Yin, B. Shen, Y. S. Kim, P. Zhang, S. Sun, J. Am. Chem. Soc. 2018, 140, 2926.
- [50] B. Han, C. E. Carlton, A. Kongkanand, R. S. Kukreja, B. R. Theobald, L. Gan, R. O'Malley, P. Strasser, F. T. Wagner, Y. Shao-Horn, *Energy Environ. Sci.* 2015. 8, 258.
- [51] L. Chong, J. G. Wen, J. Kubal, F. G. Sen, J. X. Zou, J. Greeley, M. Chan, H. Barkholtz, W. J. Ding, D. J. Liu, *Science* 2018, 362, 1276.
- [52] H. Cheng, S. Liu, Z. K. Hao, J. Y. Wang, B. J. Liu, G. Y. Liu, X. J. Wu, W. S. Chu, C. Z. Wu, Y. Xie, Chem. Sci. 2019, 10, 5589.
- [53] E. G. Luo, H. Zhang, X. Wang, L. Q. Gao, L. Y. Gong, T. Zhao, Z. Jin, J. J. Ge, Z. Jiang, C. P. Liu, W. Xing, Angew. Chem., Int. Ed. 2019, 58, 12469
- [54] S. Zhang, X. Zhang, G. Jiang, H. Zhu, S. Guo, D. Su, G. Lu, S. Sun, J. Am. Chem. Soc. 2014, 136, 7734.
- [55] M. Escudero-Escribano, P. Malacrida, M. H. Hansen, U. G. Vej-Hansen, A. Velazquez-Palenzuela, V. Tripkovic, J. Schiotz, J. Rossmeisl, I. E. L. Stephens, I. Chorkendorff, *Science* 2016, 352, 73.
- [56] M. Luo, S. Guo, Nat. Rev. Mater. 2017, 2, 17059.
- [57] J. K. Nørskov, J. Rossmeisl, A. Logadottir, L. Lindqvist, J. R. Kitchin, T. Bligaard, H. Jónsson, J. Phys. Chem. B 2004, 108, 17886.
- [58] X. Zhou, R. A. Johnson, H. N. G. Wadley, Phys. Rev. B 2004, 69, 144113.
- [59] X. Zhang, G. Lu, W. A. Curtin, Phys. Rev. B 2013, 87, 054113.